remote sensing

MDPI

Article

Bio-Optical Properties near a Coastal Convergence Zone Derived from Aircraft Remote Sensing Imagery and Modeling

Mark David Lewis [1,*], Stephanie Cayula [1], Richard W. Gould, Jr. [1,†], William David Miller [2], Igor Shulman [1], Geoffrey B. Smith [3], Travis A. Smith [1], David Wang [1] and Hemantha Wijesekera [1]

[1] Ocean Sciences Division, US Naval Research Laboratory, Stennis Space Center, MS 39529, USA; stephanie.c.cayula.civ@us.navy.mil (S.C.); rwgould891@gmail.com (R.W.G.J.); igor.g.shulman.civ@us.navy.mil (I.S.); travis.a.smith96.civ@us.navy.mil (T.A.S.); david.w.wang.civ@us.navy.mil (D.W.); hemantha.w.wijesekera.civ@us.navy.mil (H.W.)
[2] National Geospatial-Intelligence Agency (NGA) Office of Science and Methodologies (ATS), Springfield, VA 22150, USA; william.d.miller@nga.mil
[3] Remote Sensing Division, US Naval Research Laboratory, Washington, DC 20375, USA; geoffrey.b.smith4.civ@us.navy.mil
* Correspondence: mark.d.lewis54.civ@us.navy.mil; Tel.: +1-228-688-5280
† Retired.

Abstract: Bio-optical and physical measurements were collected in the Mississippi Sound (Northern Gulf of Mexico) during the spring of 2018 as part of the Integrated Coastal Bio-Optical Dynamics project. The goal was to examine the impact of atmospheric and tidal fronts on fine-scale physical and bio-optical property distributions in a shallow, dynamic, coastal environment. During a 25-day experiment, eight moorings were deployed in the vicinity of a frontal zone. For a one-week period in the middle of the mooring deployment, focused ship sampling was conducted with aircraft and unmanned aerial vehicle overflights, acquiring hyperspectral optical and thermal data. The personnel in the aircraft located visible color fronts indicating the convergence of two water masses and directed the ship to the front. Dye releases were performed on opposite sides of a front, and coincident aircraft and unmanned aerial vehicle overflights were collected to facilitate visualization of advection/mixing/dispersion processes. Radiometric calibration of the optical hyperspectral sensor was performed. Empirical Line Calibration was also performed to atmospherically correct the aircraft imagery using in situ remote sensing reflectance measurements as calibration sources. Bio-optical properties were subsequently derived from the atmospherically corrected aircraft and unmanned aerial vehicle imagery using the Naval Research Laboratory Automated Processing System.

Keywords: convergence zones; coastal; bio-optics; airborne remote sensing; atmospheric correction; circulation

Citation: Lewis, M.D.; Cayula, S.; Gould, R.W., Jr.; Miller, W.D.; Shulman, I.; Smith, G.B.; Smith, T.A.; Wang, D.; Wijesekera, H. Bio-Optical Properties near a Coastal Convergence Zone Derived from Aircraft Remote Sensing Imagery and Modeling. *Remote Sens.* **2024**, *16*, 1965. https://doi.org/10.3390/rs16111965

Academic Editor: Gad Levy

Received: 30 April 2024
Accepted: 23 May 2024
Published: 30 May 2024

1. Introduction

Convergence zones created by opposing winds and tidal forcing are important features of the coastal zone. These coastal ocean fronts contribute to sediment transport and the ecosystem for aquatic biology. In March and April of 2018, a variety of data were collected in the Mississippi Sound in and around an ocean front. A previous publication discussed the breadth of instrumentation used to collect data during these acquisitions and provided context and rationale for the study [1]. Hyperspectral remote sensing reflectance data, collected from airborne and Unmanned Aerial Vehicle (UAV) platforms, were included in this dataset. In this study, these airborne datasets were used to further analyze this front. To transform this airborne imagery into useable bio-optical properties, a series of transformations were required.

The coastal zone is the interface between land and the open ocean, and it is impacted by many processes, such as blooms, river discharge, and sediment resuspension. The

previous publication examined the impact of tides and atmospheric fronts on bio-optical variability, including the development and decay of the nepheloid layers, using mooring datasets and compared them with models [1]. Here, we expand that work to use remote sensing and modeling to further examine fine-scale coastal variability. In this paper, we will compare the coherence between fronts observed in remote sensing and fronts observed in model results. We collected extensive multi-sensor, multi-scale temporal datasets that provide a unique perspective on coastal dynamics.

The Naval Research Laboratory (NRL) has oceanographic and computational resources that provide a platform to analyze these coastal ocean datasets. NRL established the Automatic Processing System (APS) [2] based on the NASA SeaDAS application [3] to generate bio-optical products, such as chlorophyll *a* concentration and absorption coefficients, from various satellite-based remote sensors. Sensor data processed by APS includes the Visible Infrared Imaging Radiometer Suite (VIIRS) [4] and Moderate Resolution Imaging Spectrometer (MODIS) [5] data, among others. We applied the same reflectance-based bio-optical algorithms to the aircraft and UAV datasets. Model runs were performed to analyze the ability to predict these tidal and wind-driven convergence zones.

2. Methods and Data

The fieldwork was conducted in March–April 2018 in a shallow barrier island environment in the northern Gulf of Mexico (<15 m water depth)^2. The study area shown in Figure 1 was in the Mississippi Sound between Ship and Horn Islands, with upper left latitude and longitude coordinates of 30.3, −88.0, and lower right coordinates of 30.2, −88.75. After in-water sensors housed on moorings were deployed in March 2018, a variety of data were collected from a small vessel daily during the week of 04/02/18 through 04/06/18. In addition to in situ reflectance acquired at specific locations from the vessel, an aircraft collected flight lines of thermal and visible/near infrared data. In addition, during specific times, a UAV was launched from the vessel to collect small swaths of hyperspectral data. During this data collection activity on 04/05/18, personnel in the aircraft that housed thermal and reflectance sensors observed a front created during flood tide from the south and northerly winds, as shown in Figure 2b. The vessel was then directed to the front, where subsequently uranine and rhodamine dye were deployed to aid in the understanding of mixing and subduction processes [1]. Radiometer readings were taken in and around the front. Coincident measurements were taken by airborne sensors. Although in-water data were collected from sensors on the moorings, the focus of this study is the methodology used to process and analyze the above-water reflectance data acquired during the observation of the front. These data consist of in situ, airborne, and UAV datasets. Furthermore, the relationship between these datasets and model output is explored.

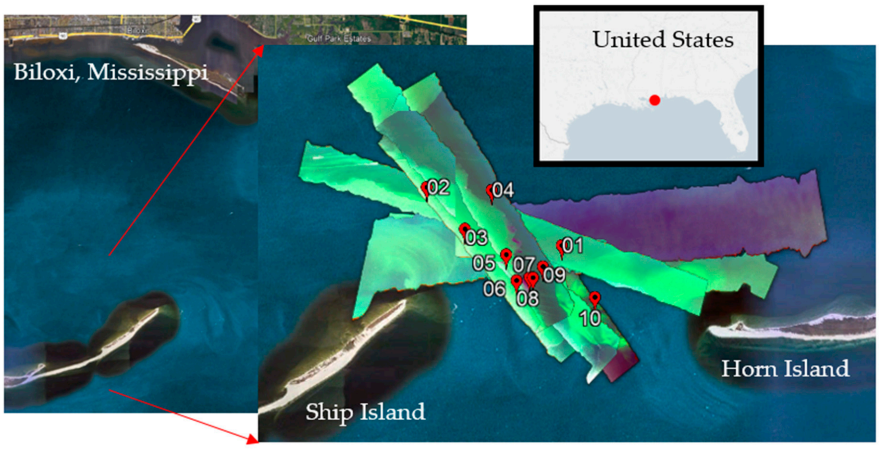

Figure 1. Study area 15 km south of Biloxi, Mississippi between Ship and Horn Islands. Enumerated in situ station locations and RGB flightlines from the μSHINE airborne hyperspectral sensor overlaid for context.

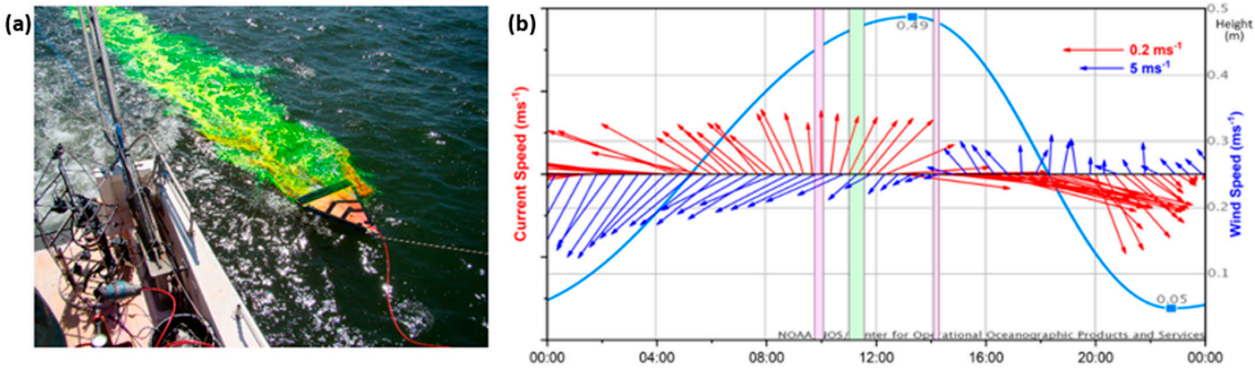

Figure 2. (**a**) Dye deployment from the R/V Wilson; (**b**) Tidal stage (blue line, height in m, right axis), winds (blue vectors), and surface currents (red vectors) on 04/05/18, during the period of three dye releases (local time, UTC-5 h). Currents are from the BP1 mooring, which was close by. Red boxes denote the times and durations of the two rhodamine releases; the green box denotes the time and duration of the single uranine release. Winds and tides from the NOAA Center for Operational Oceanographic Products and Services [6].

2.1. In Situ Data

We conducted day trips on a small vessel (R/V Wilson, operated by the Dauphin Island Sea Lab) in and out of Biloxi, Mississippi, to the study area for 5 days in the middle of the mooring deployment (04/02/18–04/06/18). The ship provided continuous, underway surface mapping and vertical profiling of physical and optical properties at specific locations.

To facilitate visualization of advection/mixing/dispersion processes near fronts, we released two different color fluorescent water-tracing dyes (rhodamine, red; uranine (also known as fluorescein); green) on 04/02/18 and 04/05/18, during the ship sampling. These dyes are commonly used in water tracing studies and are environmentally safe [7–9]. Prior to deployment, the dyes were mixed with water and isopropyl alcohol in 250-gallon tanks to densities approximating ambient surface water, to help ensure that the dye remained at the surface and did not sink (other than through mixing and advection processes) [10]. The two 250-gallon tanks (one for each dye) were secured to the deck of the R/V Wilson. The dyes were pumped through a hose, out of a boom, and down to a small vane skimming the surface. Details of the dye analysis will be discussed in future publications. The relevance of this study is that two of the in situ reflectance measurements were impacted by the dye signature and removed from the calibration activity discussed below.

For the dye release on 04/05/18, the aircraft surveyed the study area prior to the dock departure of the R/V Wilson to locate a suitable front for more detailed sampling. The aircraft directed the ship to the front, where we deployed the two dyes on the surface on opposite sides of the front. We then tracked the dyes with aircraft and UAV overflights. Figure 2a shows the hose, boom, skimming vane, and dye being used in the deployment of a uranine dye dispersal during this activity. Figure 2b shows the tidal stage, winds, and surface currents on 04/05/18, during the period of three dye releases. In the morning for the rhodamine and uranine releases, winds were from the northeast during a flood tide. In the afternoon for the second rhodamine release, winds switched to the south during an ebb tide. In both cases, the winds and tides were opposed, which is why the condition we expected was favorable to set-up the front. Following the dye releases, time-sequences of hyperspectral imagery collected by the Naval Research Laboratory (NRL) aircraft and UAV provided detailed spectral information of the water surface and clearly showed the movement of the two dyes, helping us better understand dye dispersion processes.

The in situ data source acquired for airborne sensor empirical line calibration were collected by an Analytical Spectra Devices (ASD) HandHeld 2 (HH2) visible and near-infrared (VNIR) Spectroradiometer. The configuration was preset to record 5 spectra for the sky, 5 spectra for the calibration panel, and 5 spectra for the water. The data were collected

using standard spectrometer acquisition methods, with first recording the sky spectra with the ASD HH2 oriented at 135 degrees in azimuth from the sun's position and at 40 degrees from zenith, then recording the calibration target and the water with the same azimuthal orientation [11]. The calibration target was a LabSphere SRT-10-100 Reflectance Target. Postprocessing and reflectance correction of the ASD data were performed using standard techniques established by Goddard Space Flight Space Center [12]. The location of the ASD stations are shown in Figure 1, enumerated by the order in which they were acquired.

There were 10 total ASD measurements taken on 04/05/18 at selected locations when the vessel was stationary. These stations were collected during times when the vessel stopped to turn around at the end of a dye run or when preparing to launch a UAV sensor. The postprocessing that established reflectance measurements for each ASD data collection location used an inversion algorithm that requires in-water in situ absorption at 412 nm to refine the accuracy of the reflectance measurements [13]. These in situ measurements were taken by an AC9 absorption profiler that was lowered into the water to collect absorption data at the locations of the ASD measurements.

The absorption profiler that acquired the coincident absorption measurements with the ASD measurement was a Seabird AC9 profiler. Standard procedures were used to lower the AC9 profiling cage into the water. The study area has a shallow bottom that is in the range of 2 to 5 m across the study area. The profiling cage depth was controlled by a winch to lower the profiling cage to just above the bottom and then raise it to the surface, recording absorption and attenuation through the water column. When the profiling cage nears the sea floor, sediment can be stirred up. Therefore, data selected for inclusion was collected during the downcast to avoid an increase in the inherent optical properties generated by this sediment [14].

The standard postprocessing protocol was used [15]. Temperature and salinity corrections were applied using coincident ship data. The pure water calibration was subtracted from the in situ data. Spikes due to bubbles were removed. The Zaneveld scatter correction and Pope pure water coefficients were applied [16,17].

The AC9-derived absorption coefficients at 412 nm were used to refine the corresponding ASD reflectance measurements [13], which were subsequently used as the in situ data source for calibration of the airborne datasets. In the calibration methodology described later, these refined ASD reflectance values will be called the ASD Rrs values.

2.2. Remote Sensing Imagery

Synoptic surface imagery at multiple spatial resolutions using a suite of satellite, airborne, and UAV sensors was collected. The calibration of airborne radiance data with the in situ reflectance measurements provided a methodology to generate bio-optical data products over the study area. A comparison of bio-optical data products from satellite and airborne sensors was made to validate the calibration process. Measurements from overlapping airborne-acquired bio-optical data products were then compared.

2.2.1. Satellite

Level 1 MODIS imagery (1 km and 250 m spatial resolution) was downloaded from the NASA LAADS web site (https://ladsweb.modaps.eosdis.nasa.gov (accessed on 30 April 2024)) and Level 1 VIIRS imagery (750 m spatial resolution) was available from the NOAA Comprehensive Large Array-Data Stewardship System (CLASS) web site (www.class.noaa.gov). Both the MODIS and VIIRS imagery were processed through the NRL APS [2] to atmospherically correct the data and produce bio-optical products (such as chlorophyll *a* concentration, absorption, backscattering, and attenuation coefficients) using algorithms consistent with standard NASA SeaDAS processing [3,18]. These bio-optical image products provide large-scale spatial context for oceanographic features. Relevant information for the VIIRS data used in the study is included in Table 1.

Table 1. Sensor characteristics for VIIRS data used in study.

Spectral Range (nm)	Number of Bands	FWHM (nm)	Pixels (Row × Col)	Altitude (km)	Resolution (Meter)
410, 443, 486, 551, 671, 745, 862	7	20 nm excluding 745 and 862 nm	400 × 800	829	750

2.2.2. Aircraft

Aircraft overflights with onboard visible, near-infrared (VNIR) sensors acquired data across the entire sampling area over the 6-day period (04/01/18–04/06/18) to provide spatial context for the ship sampling and to provide high temporal and spatial resolution coverage. Flight paths were coordinated with the ship surveys, and the aircraft crew helped direct the ship to appropriate sampling locations near fronts.

NRL flew a Twin Otter aircraft (Canadian de Havilland DHC-6) equipped with several sensors, including the compact μSHINE visible–near-infrared (VNIR) hyperspectral imaging sensors developed at NRL [9]. The μSHINE sensor was mounted on a computer-controlled 2-axis gimbal that provided pointing capabilities both for glint mitigation and longer dwell-time observations. Navigation was recorded on a Systron Donner CMigits III (10 Hz sampling frequency and 0.05°/3.9 m resolution) and used for geocorrection of sensors on the gimbal. Specifications of the μSHINE system are shown in Table 2. The altitude of the aircraft for the flight lines was approximately 2000 m, which results in about a 1.3 m spatial resolution.

Table 2. Sensor characteristics for NRL μSHINE cameras flown on Twin. FWHM = Full Width Half Maximum, FOV = Field of View.

Spectral Range (nm)	Number of Bands	FWHM (nm)	Pixels	Framerate (Hz)	FOV (°)	Bit Depth	Altitude (Meter)	Resolution (Meter)
319–1000	136	5.0	1360	40	48	12	2000	1

Overpasses were conducted roughly every 6 min for approximately 6 h of flight time each day (from approximately 08:30–11:30 to 13:30–16:30 local time), with a 1 m spatial resolution. There were 150 flight lines of data collected during the experiment, covering 1325 linear kilometers. At typical flight altitude and view geometry (1100 m and 40°), this resulted in approximately 1060 km^2 of imagery. A photo of the dye release taken from the aircraft on 4/5 is shown in Figure 3. The μSHINE data provided the airborne radiance measurements for this study on 04/05/18.

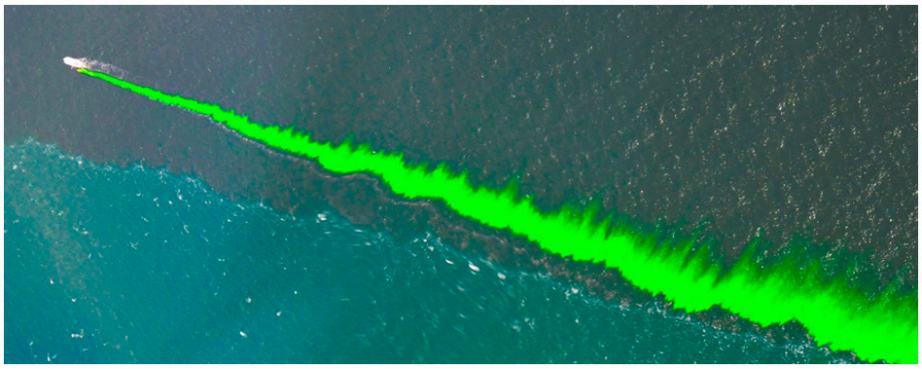

Figure 3. Uranine dye deployment around 1600 UTC on 04/05/18; view from the NRL aircraft. Note the front between the offshore waters at the bottom of the image (south) and the coastal waters at the top of the image (north). Fine-scale diffusive features are apparent in the dye distribution within minutes of the dye release.

2.2.3. UAV

PrecisionHawk, Inc. (Raleigh, NC, USA) was contracted to collect Unmanned Aerial Vehicle (UAV) imagery during the field campaign. Three small UAVs were launched and returned to the R/V Wilson at various times during the day. One of the UAVs was equipped with a red-green-blue (RGB) Phantom 4 Pro camera and helped to visually identify frontal locations and track/map the dye plumes, which facilitated adaptive sampling during the field experiment. Two other UAVs, one equipped with a blue-green-NIR (BGNIR) Zenmuse X5 camera on a Matrice 100 platform and one with a hyperspectral Headwall Nano-Hyperspectral sensor on a Matrice 600 platform, provided more detailed spectral information of the water surface to help better understand dispersion of the dyes and to enable estimation of fine-scale water bio-optical properties. 1.5 TB of still photography and video from the UAVs were collected over four sampling days. Specifications of the Headwall Nano-Hyperspectral sensor used in the study are shown in Table 3.

Table 3. Sensor characteristics for headwall nano-hyperspectral sensor.

Spectral Range (nm)	Number of Bands	FWHM (nm)	Pixels	Framerate (Hz)	Bit Depth	Altitude (Meter)	Resolution (Centimeter)
400–1000	340	6.0	1024	250	12	40	1

2.3. Data Calibration and Transformation

Bio-optical products were generated from standard APS processing of the 04/05/18 VIIRS scene over the Mississippi Sound, including normalized water leaving radiance, remote sensing reflectance, backscatter, beam attenuation, and chlorophyll l *a*. In order to compare the µSHINE- and VIIRS-derived bio-optical products, several transformations and adjustments were performed on the µSHINE data. The processing steps that used navigation logging and were required to transform the raw µSHINE into a form usable by APS data include radiometric calibration, geometric correction, empirical line calibration (ELC) [19–21], convolution to the VIIRS Relative Spectral Response (RSR), and transformation to an input format that is used by APS to generate and georeferenced bio-optical products.

2.3.1. Calibration Approach

The radiometric calibration transforms the raw µSHINE digital numbers into sensor radiance measurements based on the gains established through the use of an integrating sphere conducted in an optical laboratory prior to flights. Radiometric calibration follows the protocols outlined in Davis et al. [22]. Briefly, µSHINE is placed in front of a 40-inch Spectraflect-coated integrating sphere (Labsphere Inc., North Sutton, NH, USA) containing 10 halogen lamps. The intensity of the sphere at various lamp combinations is determined by a transfer calibration from a NIST-calibrated Field Emission Lamp. A mathematical relationship between digital counts from µSHINE and sphere intensity is then generated for each pixel on the CCD for a range of sphere intensities. This transforms the raw digital values recorded by the µSHINE sensor into radiance values, preparing for the computation of water leaving radiance and other ocean color products.

The inertial navigation system (INS) on the Twin Otter provided information used to create Geographic Lookup Table (GLT) files, which provide a latitude and longitude for each pixel in the airborne imagery. The roll, pitch, and heading provided by the INS, along with the latitude, longitude, and altitude at the center point of the aircraft, were combined with sensor pointing files to create the GLT. These grids contain the location of the aircraft at the time of acquisition for each row and column in the airborne data grid and were used during the creation of the input file for APS that needs the sensor zenith and azimuth angles for each pixel of the input data grid.

Along with APS, the ENVI Image Analysis Application and Interactive Data Visualization (IDL) programming languages were used to process the µSHINE data. Much of the

processing was scripted so that batch processing of µSHINE flight lines could be performed. Flight lines of radiometrically calibrated radiance were georeferenced using the associated GLT files in ENVI/IDL.

Using the navigation and region of interest tools in the ENVI display, the ASD latitude and longitude positions were located in the imagery, and 3 × 3 pixel regions of interest were drawn around the ASD stations to extract the radiance values. The post-processed ASD Rrs values were spectrally sub-sampled to match the wavelengths of the µSHINE sensor. The spectrally sub-sampled ASD Rrs values were paired with the radiometrically calibrated µSHINE values extracted at the associated ASD station locations in order to perform the atmospheric calibration using the ELC technique [21].

Typically, sensors such as VIIRS orbit the earth at an altitude of several hundred kilometers and record the radiant flux at the top of the atmosphere (L_t). One aspect of the required processing is to remove atmospheric effects from the L_t signal. The atmospheric scattering is partitioned into several components, including the Rayleigh radiances (L_r) and aerosol radiances (L_a). Standard atmospheric correction practice calculates L_r from solar and sensor zenith and azimuth angles. A well-accepted approach for estimating L_a uses the relationship between 2 near infrared (NIR) wavelength bands or 2 short-wave infrared (SWIR) wavelength bands to select an aerosol model [23]. These models are indexed by the relative humidity and particle size fraction of the aerosol constituents. Since water absorbs in these regions, it is assumed that after the removal of L_r, any sensor-measured response in the NIR or SWIR represents atmospheric scattering. The relative humidity can be pulled from climatological data. However, the particle size fraction is inferred from the relationship between the measurements at these NIR or SWIR wavelengths, which, without aerosol contamination, should be zero in pure water. Once the particle size fraction is determined, the appropriate aerosol model can be selected based on the relative humidity and atmospheric particle size fraction index values [24].

In addition, to compensate for the drift in space-borne sensor sensitivity over time, regular in-orbit calibration activity occurs to compute sensor gain sets that fine-tune the sensors' radiometric calibration. For these satellite-based sensors, the calibration process is based on propagating in situ measured normalized water leaving radiance (nL_w) up through the atmosphere using the same solar and sensor angles as the observed signal of the satellite sensor. This yields a vicarious top of the atmosphere radiance (vL_t) which is what the sensor should record in order to produce the in situ nL_w value after atmospheric correction. The ratio of vL_t / L_t at the sensor wavelengths results in a sensor gain set for each band. The sensor L_t values are then multiplied by the sensor gain set to adjust for deviation of the sensor from its radiometric calibration due to stresses at launch and sensitivity drift over time [25,26].

However, for an aircraft at an altitude of only a few hundred meters, the recorded signal has not passed through the entire Earth's atmosphere. Therefore, the standard Rayleigh radiance (L_r) and aerosol radiance (L_a) from the aerosol model lookup tables are not appropriate for computing the L_r and L_a radiance values to subtract from L_t. Vicarious calibration is also not appropriate since it relies on a good approximation of the L_r and L_a values. Therefore, even though a limited amount of atmospheric effect exists, there is enough light scattering to require alternate atmospheric correction approaches to be considered, in addition to the standard radiometric calibration. The atmospheric correction approach taken in this study builds on the ELC by using coincident in situ radiometer data acquired from a vessel on the water at the time of the overpass flight.

The calibration generated from the ELC is a regression that maps from the domain of the radiometrically calibrated µSHINE radiance to the range of the "true" reflectance represented by the in situ ASD Rrs values. Of the ten ASD radiometer measurements taken on 04/05/18, two were recorded in the dye release and therefore were not usable in the ELC process. Even though the time between ASD and µSHINE data acquisition was less than 5 min for these locations, the movement of the dye in the water was fast and tainted the spectral matchups. Figure 4a shows the radiance measured by µSHINE at ASD station 1

as a baseline example of a radiance measurement without dye contamination. The plots in Figure 4b,c, show the µSHINE data at ASD locations 2 and 7 that were contaminated by the dye reflectance. The µSHINE data at station 2 had a spike at 500 nm from the uranine dye. The µSHINE data at station 7 had a spike at 595 nm from the rhodamine dye. Therefore, these matchups were not used for the ELC.

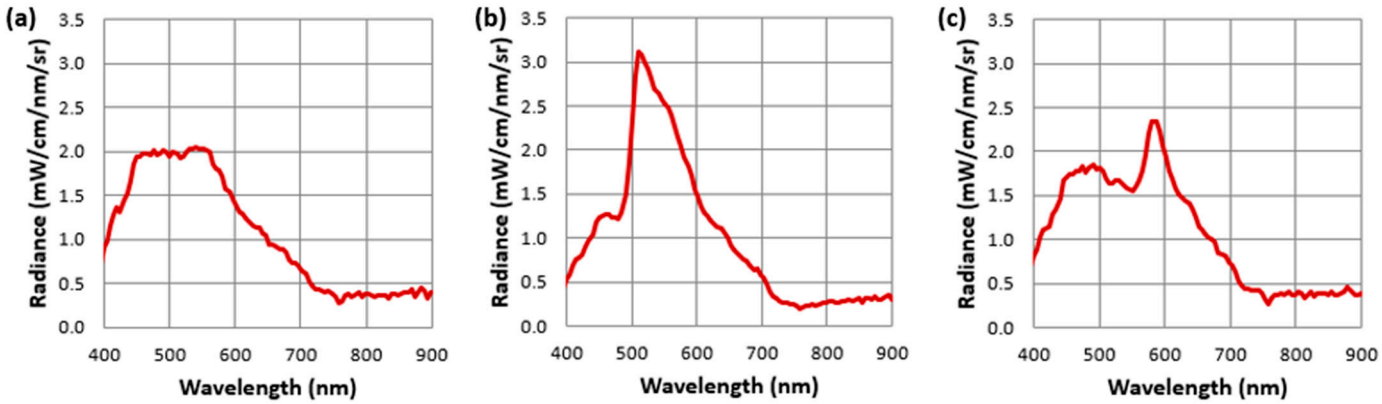

Figure 4. µSHINE radiance measurements at (**a**) ASD station 1 with no dye contamination, (**b**) ASD station 2 with uranine dye contamination, and (**c**) ASD station 7 with rhodamine dye contamination.

2.3.2. Calibration Computation

As a result, eight ASD Rrs and radiometrically calibrated µSHINE radiance value pairs were used in the regression. Ideally, the range of data points in the calibration would use multiple points across the sensor's dynamic range. Unfortunately, the logistics of collecting ASD measurements at the vessel's location resulted in data values that did not span the breadth of the µSHINE sensor's dynamic range. More measurements (stations) across the dynamic range would be better. However, these acquisitions were what time permitted. Even with more time, the dynamic range of reflectance from the water was also limited, and its distribution was not easily visually discernible. The values from these stations were what were available to use in the ELC.

Therefore, the ELC regression was forced through the origin, representing the fundamental expectation that a µSHINE radiance value of zero should pair with an ASD Rrs value of zero.

The interpolated spectral resolution of the ASD sensor is 1 nm, while that of the µSHINE sensor is 3.7 nm. Therefore, the ASD sensor values used for the regression were convolved spectrally to the µSHINE wavelengths and constrained to the range of 400 to 900 nm. Let

$x_{i,j}$ = radiometrically calibrated µSHINE radiance value at the i_{th} ASD station and j_{th} µSHINE band

$y_{i,j}$ = ASDR rsreflectance value at the i_{th} ASD station and wavlength that matches the j_{th} µSHINE band

Lab_Calibrated _µSHINE$_{r,c,j}$ = radiometrically calibrated µSHINE radiance at the r_{th} image row, c_{th} imagecolumn and j_{th} µSHINE band

ELC_Calibrated _µSHINE$_{r,c,j}$
= ELC Calibrated µSHINE reflectance at the r_{th} image row, c_{th} image column and j_{th} µSHINE band

In order to perform this calibration, the least square m_j values were computed such that $\min \sum_{i=1}^{n} \left(y_{I,j} - (m_j * x_{i,j}) \right)^2$, where n = 8 represents the number of ASD stations

The solution to the above minimization is:

$$m_j = \sum_{i=1}^{n} \left(x_{i,j} * y_{i,j}\right) / \sum_{i=1}^{n} \left(x_{i,j} * x_{i,j}\right)$$

Once the m_j values were generated, the atmospheric correction for µSHINE scenes was computed for each row (r), column (c) and wavelength band (j) of the radiometrically calibrated data grids with the equation,

$$\text{ELC\_Calibrated\_µSHINE}_{r,c,j} = \left(m_j * \text{ Lab\_Calibrated\_µSHINE}_{r,c,j}\right)$$

The APS applies several bio-optical inversion algorithms to generate ocean color products. The coefficients for these algorithms are based on the wavelengths and bandwidths of the traditional multispectral sensors. Therefore, in order to calculate bio-optical properties from the hyperspectral µSHINE imagery using the multispectral algorithms, the radiometrically calibrated and atmospherically corrected µSHINE reflectance (hereafter simply referred to as µSHINE reflectance) values were convolved to the VIIRS wavelengths based on the VIIRS relative spectral response. This process allowed us to assess the validity of the entire data transformation and bio-optical product accuracy.

Let,

$$\text{VIIRS\_RSR}_{v,j} = \text{VIIRS Relative Spectral Response for each VIIRS band } v \text{ across the } j \text{ bands of µSHINE wavelengths}$$

$$\text{Convolved\_µSHINE}_{r,c,v} = \text{µSHINE convolved to the VIIRS Relative Spectral Response at the } r_{th} \text{ image row, } c_{th} \text{ image column and } v_{th}\ VIIRS \text{ band}$$

This convolution is performed by,

$$\text{Convolved\_µSHINE}_{r,c,v} = \frac{\sum_{j=1}^{n} \text{VIIRS\_RSR}_{\text{v,j}} * ELC\_SHINE_{r,c,j}}{\sum_{j=1}^{n} \text{VIIRS\_RSR}_{\text{v,j}}}$$

For satellite-based sensors, the L_t values, along with solar and sensor zenith and azimuth angles, are stored in a Level 1 (L1) file. By default, APS reads the data from the L1 file and performs the atmospheric correction by computing the L_r, L_a and other radiances that are typically subtracted from the L_t value to compute the L_w and nL_w values. The nL_w values are then divided by the solar irradiance to calculate the remote sensing reflectance R_{rs} values. The nL_w and R_{rs} measurements at the various sensor wavelengths are used to generate almost all bio-optical products computed by APS. The atmospherically corrected nL_w and R_{rs} data along with any desired bio-optical products are written into a Level 2 (L2) file. Since the ELC performs the atmospheric removal, a methodology for introducing the nL_w and R_{rs} values to APS that circumvents the standard atmospheric correction process had to be used. This requires the convolved_$SHINE$ reflectance stored in an ENVI format to be reformatted into a pseudo-Level 2 (L2) file in a pre-designated HDF (Hierarchical Data Format) structure. The L2 file generally contains all the atmospherically corrected reflectance, radiance, and bio-optical products. The pseudo-L2 file contains the atmospherically corrected nL_w and R_{rs} values but contains no bio-optical products. The methodology that generates the pseudo-L2 file uses the geometrically corrected grids containing the aircraft location for each row and column in the input data file in order to generate sensor zenith and azimuth angles. The solar zenith and azimuth angles were calculated from publicly available ephemeris algorithms [27]. The sensor zenith and azimuth angles were computed from the aircraft navigational data. Other required information, such as the latitude and longitude grids, coefficients of solar irradiance by wavelength, a_w (water wavelength absorption coefficients) and bb_w (backscatter wavelength coefficients) were written to this pseudo-L2 file.

When APS runs on the pseudo-L2 file, it reads a flag that indicates it should skip atmospheric correction. It then proceeds to the generation of bio-optical products using

standard APS algorithms. There are many products that APS can generate, including chlorophyll *a*, beam attenuation, back scatter, absorption coefficients of detritus, and phytoplankton. The final step maps these products onto a common geographic coordinate system (latitude and longitude grids) to create Level 3 (L3) files so that data values extracted from products at the same location of overlapping µSHINE flight lines can be compared. Therefore, data values from coincident µSHINE and VIIRS L3 product files can be extracted and compared.

The ELC process was also performed for some of the hyperspectral Headwall Nano-Hyperspec sensor data, hereafter simply referred to as UAV data. Because the data are hyperspectral and have a spatial resolution of 0.035 m (35 mm), the file sizes are quite large. To accommodate this and the fact that the data were stored on an internal disk during flight, the acquired data were broken into many separate tiles and stored on a UAV-mounted data storage device. Figure 5 shows the µSHINE flight line for 17:03:28 UTC, which is 12 km long. The flight path of the UAV is represented by the red line within the µSHINE image. A total of 111 individual UAV tiles were acquired along the UAV flight path, each with varying sizes. These tiles are all separated and, therefore, do not represent one large connected geographic section. The UAV tiles are very small in comparison to the µSHINE flightline. One of the largest UAV tiles is about 130 m long, which covers only about 1% of the associated µSHINE. Therefore, all measurements of reflectance and derived products within the tile are very homogeneous. These UAV tiles are so small that extensive processing and mosaicking would be required for them to participate in a comprehensive analysis. Even though these UAV tiles are so small that they may not be able to contribute to an analysis of the much larger frontal region, this calibration methodology is shown as an approach for processing larger tiles of UAV data in future studies where overlapping image data are available.

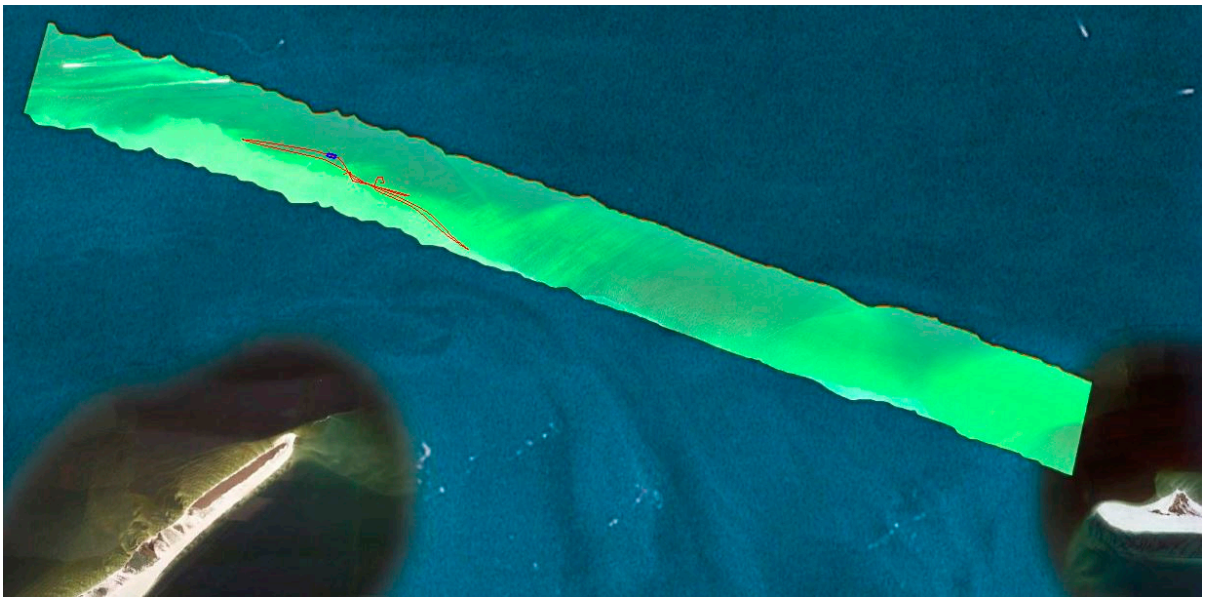

Figure 5. µSHINE flight line at 17:03:28 UTC with red track showing the flight of the UAV and the blue box showing the size of one of the largest UAV image tiles.

2.4. Model: Coupled Ocean/Atmosphere Mesoscale Prediction System (COAMPS)

The hydrodynamic model in this study is the Coupled Ocean/Atmosphere Mesoscale Prediction System (COAMPS) [1]. This is the three-dimensional hydrodynamic model with a 50 m resolution and 50 vertical levels. The bathymetry was derived from the NOAA 3-s (90 m) Coastal Relief Model (CRM) [28] dataset. The model provided predictions of temperature, salinity, and currents during the spring of 2018 and for the area covering the deployment of remote sensing observational assets described in the previous sections. To

identify and locate fronts in the model predictions, we estimated surface current properties such as curl, divergence, and strain (all normalized by Coriolis parameter f). High values in these properties (positive or negative) indicate locations of strong current convergence or divergence that might be indicators of frontal structure locations separating different water masses.

3. Results

3.1. ELC Results–Aircraft Imagery

The ELC was performed using the ASD-derived Rrs values for each µSHINE wavelength at the 8 ASD acquisition location. The µSHINE sensor has an approximate 5 nm bandwidth. Therefore, the ELC was performed at 5 nm intervals, covering the wavelength range from 400 to 900 nm. The closest µSHINE flightline in time to the ASD acquisition time was used for the pairing. On average, the time difference between the ASD acquisition and the µSHINE acquisition for each matchup point was 35 min. Ideally, they would be acquired at exactly the same time. However, the logistics of managing two separate acquisitions, one from the aircraft and one from the vessel, impacted the ability to have them acquired at the exact same time.

The VIIRS scene acquired on 04/05/18 at 19:13:59 UTC is used in the comparison plots below. This scene is cloud-free around the study region. The chlorophyll l *a* product from this VIIRS scene is shown in Figure 6.

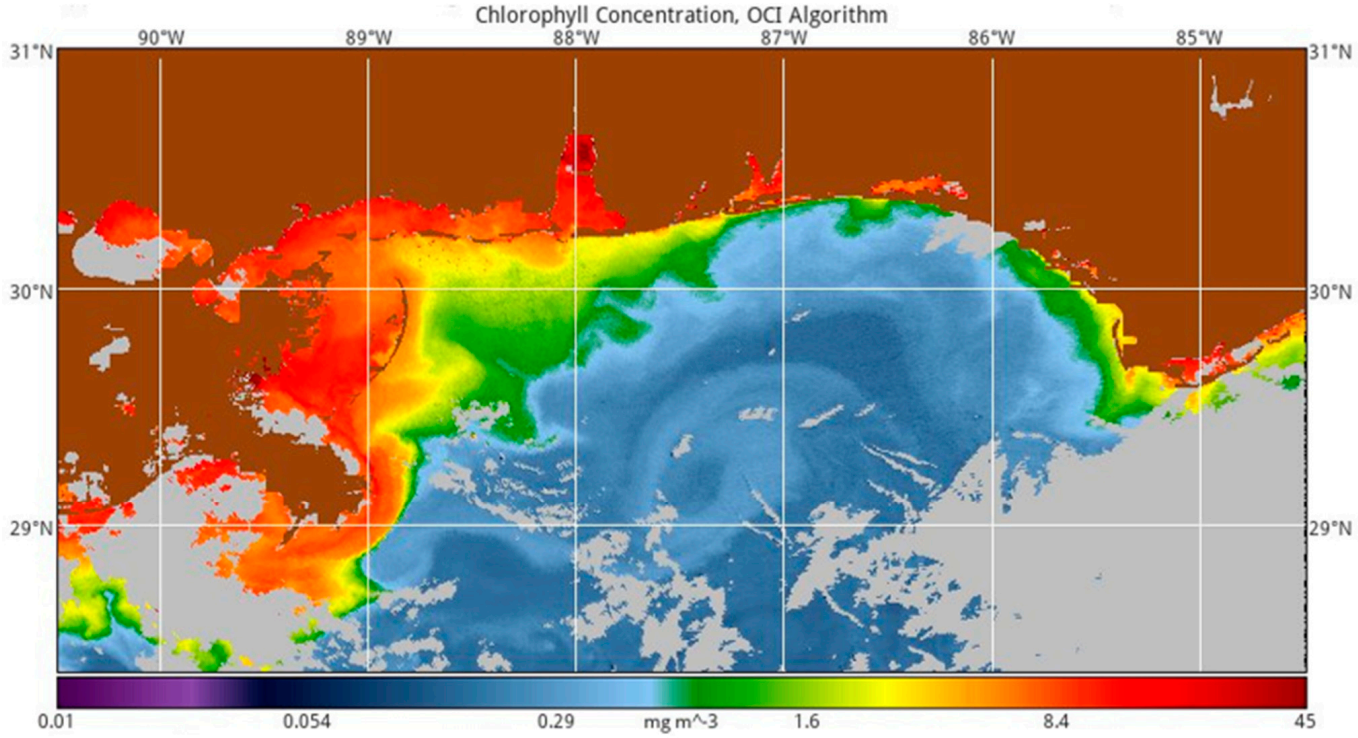

Figure 6. Chlorophyll a from VIIRS scene acquired on 04/05/18 at 19:13:59 UTC.

The results of the calibration are shown in Figure 7. The rise of the radiometrically calibrated spectra in the blue and NIR regions represents atmospheric light scattering that is corrected by the ELC. The ELC procedure uses a regression model approach across all µSHINE wavelengths and acquisition stations, so some biases remain. Since the regression model includes the eight data pairs at each wavelength, it will not be a perfect conversion from the µSHINE radiance to the ASD reflectance at each individual station. However, the results show a good approximation to the ASD reflectance at the collection of in situ stations.

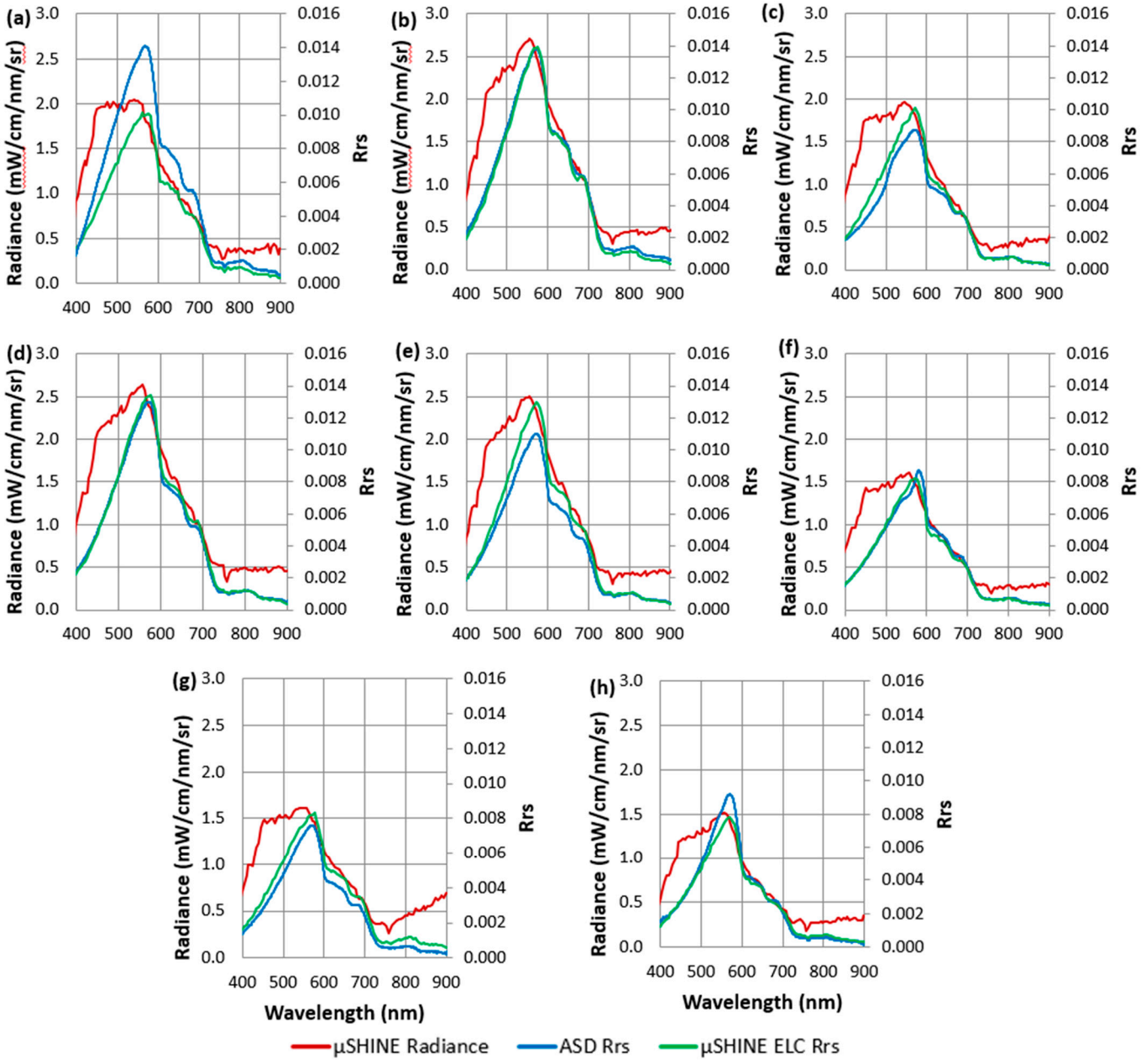

Figure 7. ASD, Radiometrically Calibrated μSHINE Radiance, and μSHINE ELC Remote Sensing Reflectance (Rrs) at locations for ASD stations 1, 3, 4, 5, 6, 8, 9, 10 identified as (**a**–**h**), respectively. μSHINE Radiance uses the left y-axis, while μSHINE ELC Rrs and ASD Rrs use the right *y*-axis.

The gains created through the ELC process were then applied to all the pixels in 19 different μSHINE flight line images to generate atmospherically corrected μSHINE R_{rs} datasets. These hyperspectral flight lines were then convolved with the VIIRS Relative Spectral Response (RSR) to simulate VIIRS data from the μSHINE data. The ASD measurements, along with the actual VIIRS R_{rs} and convolved μSHINE data that simulate the VIIRS R_{rs} are shown in Figure 8.

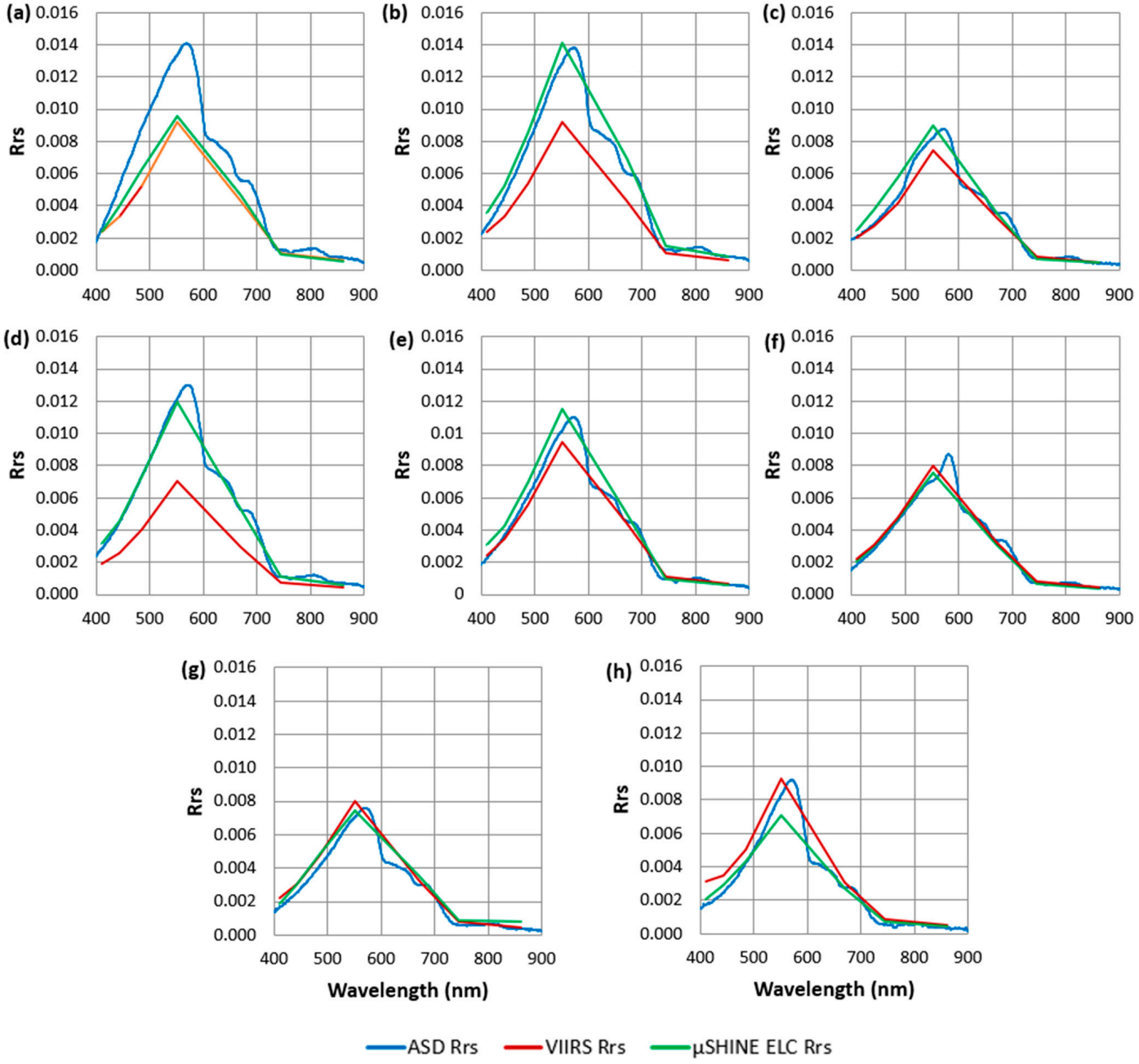

Figure 8. ASD, VIIRS, and simulated VIIRS from µSHINE ELC Remote Sensing Reflectance (Rrs) at ASD stations 1, 3, 4, 5, 6, 8, 9, 10 identified as (**a**–**h**), respectively.

3.2. Bio-Optical Property Distributions (APS Results)

These simulated VIIRS R_{rs} datasets were converted to nL_w and packaged so that APS would process them as already atmospherically corrected nL_w values. Several different bio-optical products were generated from these datasets, including chlorophyll *a*, backscatter, and absorption. The plots in Figure 9 show the matchups between the chlorophyll *a* product generated from the VIIRS and µSHINE simulated VIIRS datasets. The plot in Figure 9a shows the chlorophyll *a* matchups at the eight ASD station locations used in the ELC. In this comparison, the times of each ASD measurement at the eight stations are paired with the µSHINE measurement at the acquisition time closest to the associated ASD data. As a result, the VIIRS chlorophyll *a*, which was acquired at 19:13:59 UTC, is paired with µSHINE chlorophyll *a*, acquired up to 4 h earlier and 2.5 h later than the VIIRS data. To create a comparison for chlorophyll *a* without this time variation, a grid at the

VIIRS 750 m resolution was created over the µSHINE acquired at 19:17:17 UTC. This is the temporally closest µSHINE flight line to the VIIRS overpass. The chlorophyll *a* values from this single µSHINE flight line are plotted against the co-located VIIRS chlorophyll *a* in Figure 9b. Where multiple µSHINE grid locations fell within one VIIRS grid cell, the mean of the µSHINE chlorophyll *a* values was used to create a unique matchup with the VIIRS chlorophyll *a* value in that grid cell.

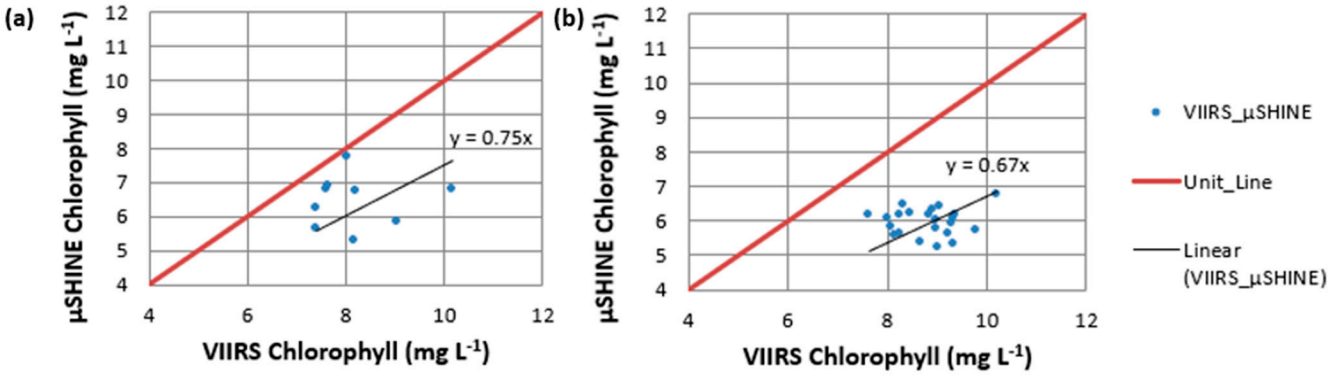

Figure 9. Chlorophyll a matchups between VIIRS convolved µSHINE data and VIIRS acquired on 04/05/21 at 19:13:59 UTC for (**a**) 8 ASD locations collected across several µSHINE flight lines and (**b**) VIIRS grid locations from the µSHINE flight line acquired on 04/05/21 at 19:17:17 UTC.

Neither the VIIRS nor µSHINE chlorophyll *a* data values cover much of the full potential dynamic range of chlorophyll *a*. Therefore, the trend line shown in these plots was forced through the origin, since both chlorophyll *a* measurements should converge at zero. Also, the RMSE was used as a metric of accuracy. In both plots, the µSHINE chlorophyll *a* values underestimated the VIIRS chlorophyll *a* values. The VIIRS and µSHINE chlorophyll *a* matchups at the ASD locations in Figure 9a have a slope of 0.75. The RMSE for the matchups at the ASD locations is 2.31. The matchups at the grid locations collocated in time in Figure 9b have a slope of 0.67. The RMSE for the matchups at the VIIRS grid locations is 2.97 mgL^{-3}. The Mean Absolute Error (MAE) is 2.88 mgL^{-3}.

It should be noted that the µSHINE flight line at 19:17:17 UTC used in the grid matchup was not used in the data pairing that generated the ELC gains. Therefore, it is truly independent and does not introduce any bias in the calibration transformation.

3.3. ELC Results–UAV Imagery

The ELC process removed atmospheric effects from several of the radiometrically calibrated µSHINE datasets. Then, the ELC µSHINE data were transformed and processed by APS to generate bio-optical ocean color products. The images in Figure 10 show the phytoplankton absorption (aph) measured by the µSHINE at 443 nm. Images of the µSHINE-measured chlorophyll *a* corresponding to these flight lines are shown in Figure 11.

In addition, the ELC µSHINE data were used as surrogate in situ data to atmospherically correct the raw reflectance data from selected image tiles collected by the UAV. The initial radiometric calibration was performed for these tiles. However, the calibration panels used were panels of different reflectance materials on the deck of the vessel. While this initial calibration did transform the raw data into reflectance units, those panels were acquired from the pitching deck, and further calibration using the ELC method was required. One of these processed tiles that was collected at 17:16:00 UTC is represented by the blue polygon in Figure 5. The tile's reflectance data were calibrated using the ELC, and then bio-optical ocean color products were generated with APS. Locations at each corner of the 130 m long UAV tile were selected. The corresponding point in the 12 km long µSHINE flight line acquired at 17:03:28 UTC was used. The ELC µSHINE Rrs data at these points were pairs with the corresponding raw UAV reflectance data. The ELC process was then performed to generate the ELC UAV dataset. This ELC UAV data were processed by APS

to generate bio-optical ocean color products. Images of this UAV tile's chlorophyll *a* and phytoplankton absorption at 443 nm are shown in Figure 12. The black pixels in the images are locations where the ocean product data values spike outside the display range due to glints and white-caps in the UAV scene.

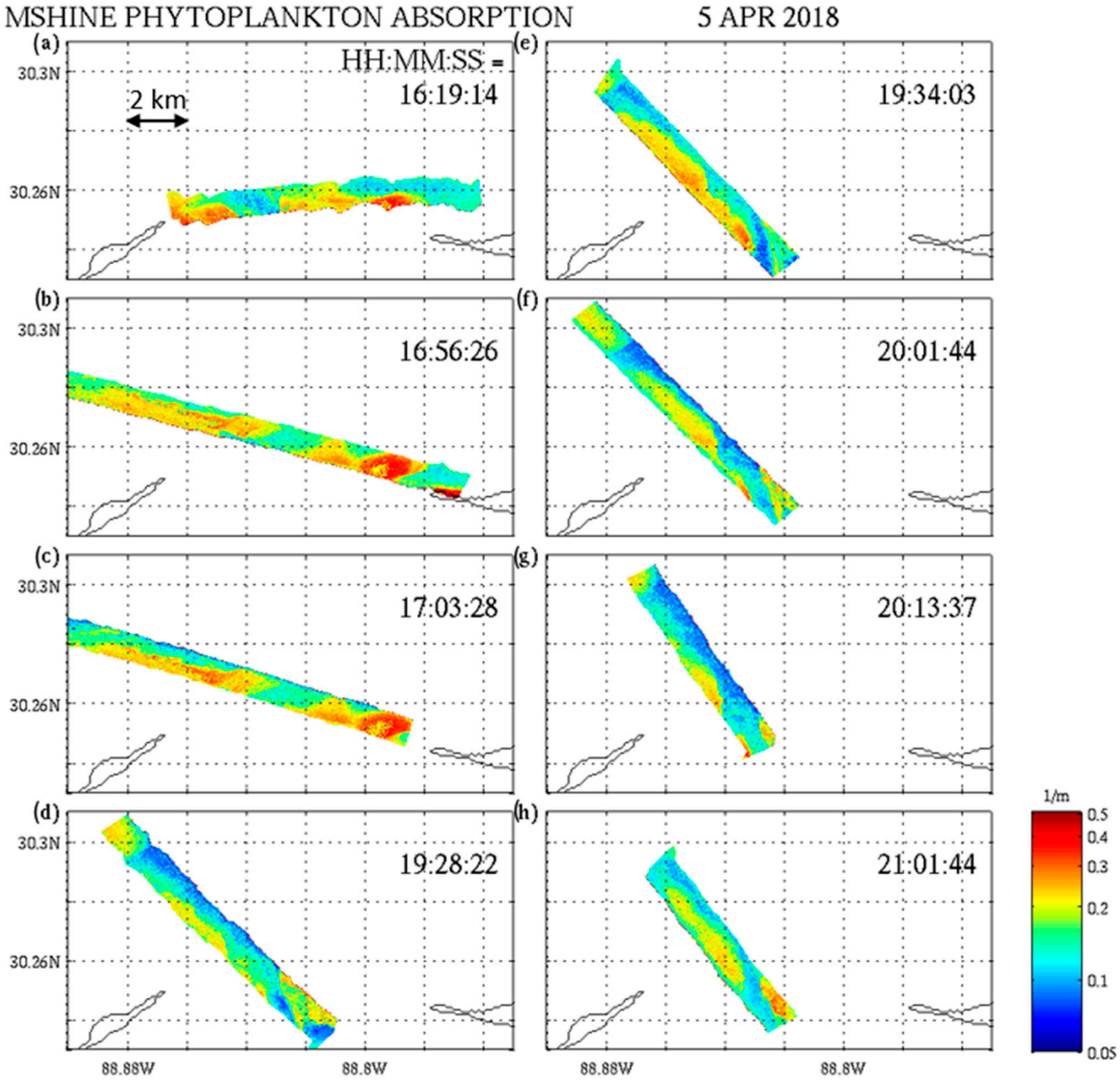

Figure 10. (**a**–**h**) μSHINE phytoplankton absorption in units of mg/m^3 of the rotating convergence zone from the predominately east-west orientation at 16:19:14 UTC in (**a**) through several flightlines and ending in the predominately north-south orientation at 21:01:44 UTC (**h**).

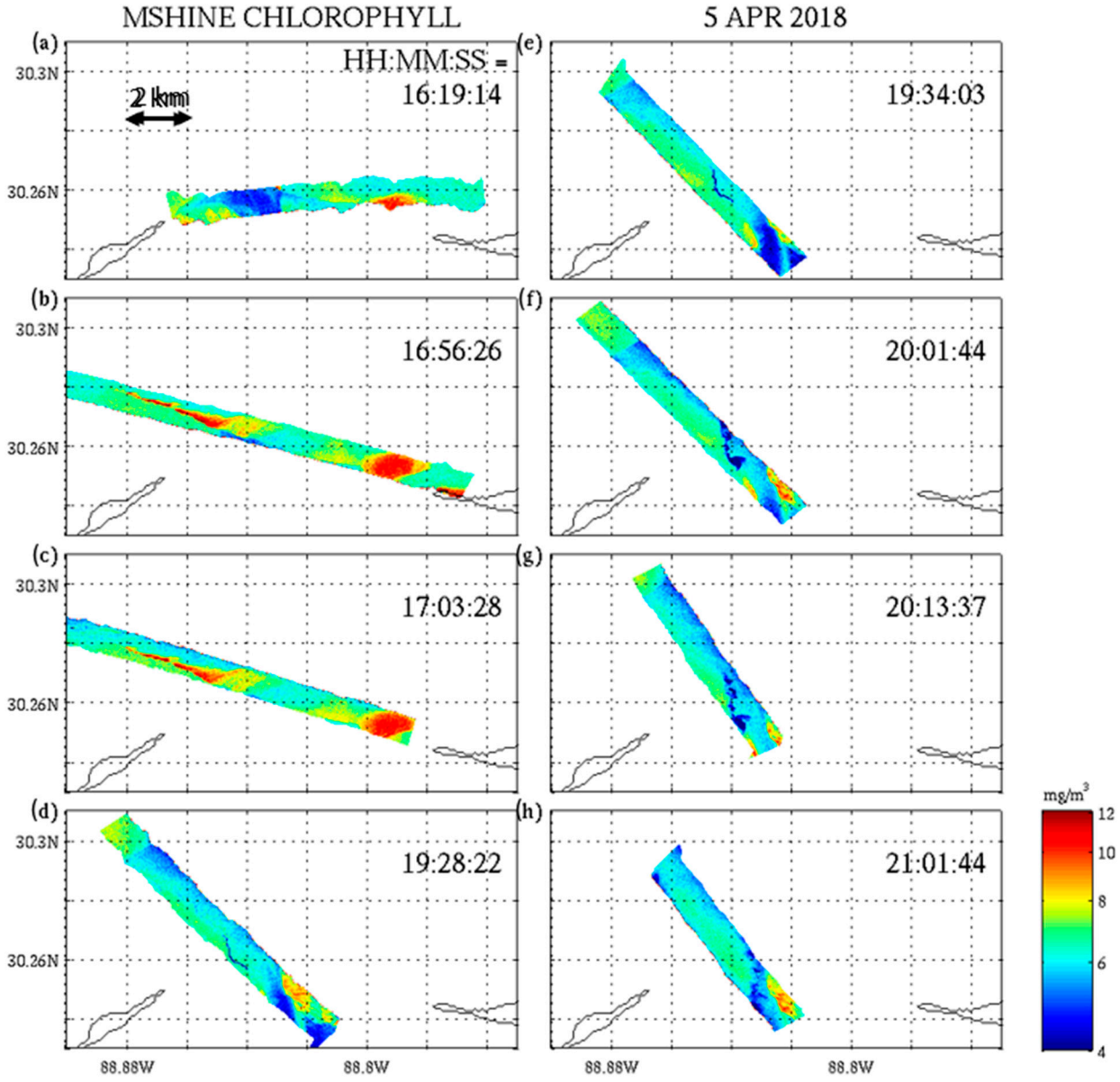

Figure 11. (**a**–**h**) μSHINE chlorophyll a in units of mg/m^3 of the rotating convergence zone from the predominately east-west orientation at 16:19:14 UTC in (**a**) through several flightlines and ending in the predominately north-south orientation at 21:01:44 UTC (**h**).

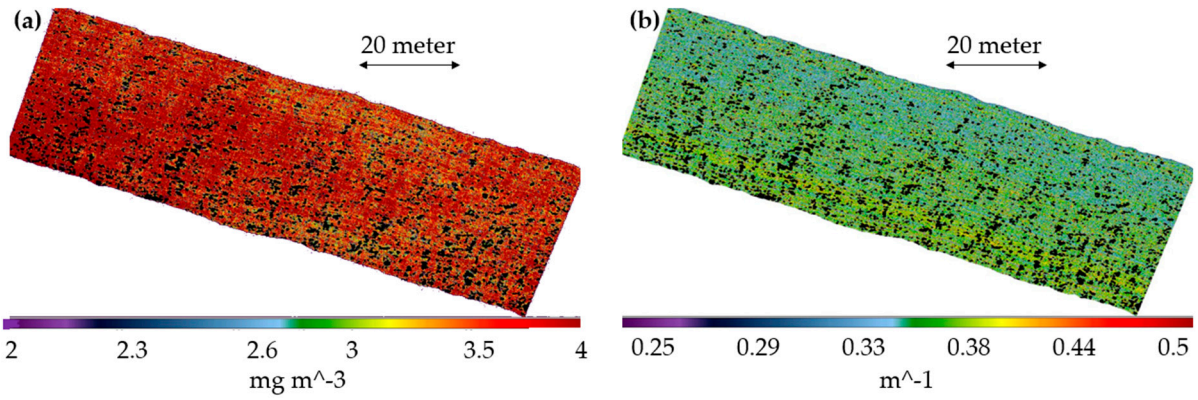

Figure 12. UAV 17:16:00 UTC tile's bio-optical ocean color products: (**a**) total absorption at 443 nm, (**b**) chlorophyll a (right).

4. Discussion

The primary data source used for analysis is the μSHINE data. The VIIRS satellite data were used in the validation of the calibration approach for the aircraft's μSHINE data. At 750 m spatial resolution, the VIIRS data are not well suited for exploring the finer scale convergence boundary. The UAV tiles were too small and homogeneous to comprehensively participate in the analysis. The description of the UAV tile calibration was included to demonstrate the validity of this calibration approach using the μSHINE data as surrogate calibration in situ data.

The images in Figure 10 show that the phytoplankton absorption (aph) measured by the μSHINE at 443 nm indicates that the aph has values of 0.2 through 0.5 (yellow through red) on the colder saline side of the front and aph values of 0.05 through 0.2 on the warm freshwater side of the front. This relationship is maintained as the front rotates during the time period of the tide and wind transition.

The chlorophyll *a* measured by μSHINE in Figure 11 shows the biological activity on the upwelling cold side of the front as it transitions through the day. Some of the rhodamine dye is evident in the chlorophyll *a* as linear blue and dispersed blue features. The chlorophyll *a* values on the colder, more saline side of the front are between 6 and 12 mg/m^3, while those values are less than 6 mg/m^3 on the warm lower saline side of the front.

The model showed that there was a strong stratification at the beginning of the wind reversal, with a well-defined two-layer system in salinity. As upwelling and surface cooling continued, the two-layer system completely collapsed to well-mixed or very weakly stratified water columns in the modeling domain around islands, as well as to the north and south of islands[2]. This formed and sharpened the front observed also by aircraft imagery and by the Wilson surveys during 5 April, as shown in Figure 3. The results show that locations of R/V Wilson (sampling of the observed front), flight lines along the front, and high values of curl, divergence, and strain (from the hydrodynamics model) coincide in the area where the front was observed by different imagery assets during surveys on 04/05/2018.

The COAMPS model was able to reproduce the wind reversal from downwelling to upwelling favorable winds (north-westward winds) presented in Figure 2b on 04/05/2018. The model showed that there was a strong stratification at the beginning of the wind reversal, with a well-defined two-layer system in salinity. As upwelling and surface cooling continued, the two-layer system completely collapsed to well-mixed or very weakly stratified water columns in the modeling domain around islands, as well as to the north and south of islands[2]. This formed and sharpened the front observed also by aircraft imagery and by the Wilson surveys during 5 April (Figure 13). The results show that locations of R/V Wilson (sampling of the observed front), flight lines along the front, and high values of curl, divergence, and strain (from the hydrodynamics model) coincide in the area where the front was observed by different imagery assets during surveys on 04/05/18.

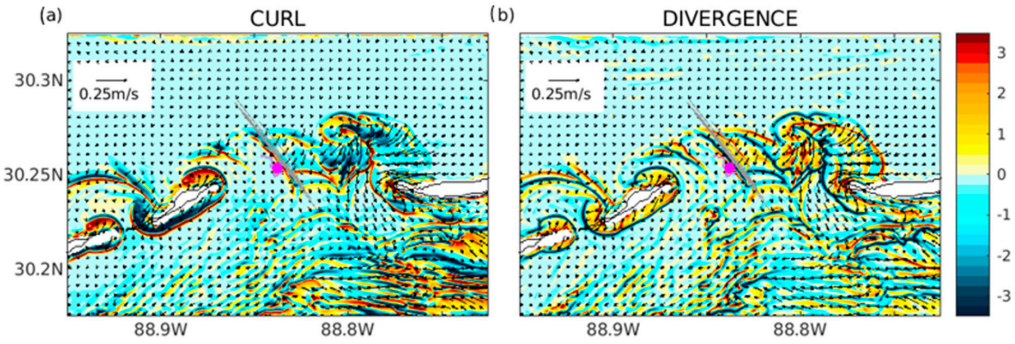

Figure 13. Estimated curl (**a**) and divergence (**b**) (normalized by the Coriolis parameter f) from the hydrodynamic model overlaid by locations of aircraft flights and the R/V Wilson location on 04/05/2018

at 20:00:00 UTC: color bars represent magnitudes of curl (**a**) and divergence (**b**); aircraft flight locations are shown with gray lines, and the R/V Wilson location is shown with a magenta circle.

We also estimated current properties (curl, divergence, and strain normalized by Coriolis parameter f) for 49 h averaged model surface currents. The intent was to remove influences from tides, diurnal atmospheric forcing oscillations, and inertial oscillations. This allows us to investigate if submesoscale processes like, for example, surface frontogenesis contributed to the formation of the front detected by surveys. Magnitudes of curl/f (which is called the Rossby number) and strain/f for 49 h averaged surface currents were reaching magnitudes above 1 in the area of the front, which indicate that submesoscale processes contributed to the front formation, as shown in Figure 14.

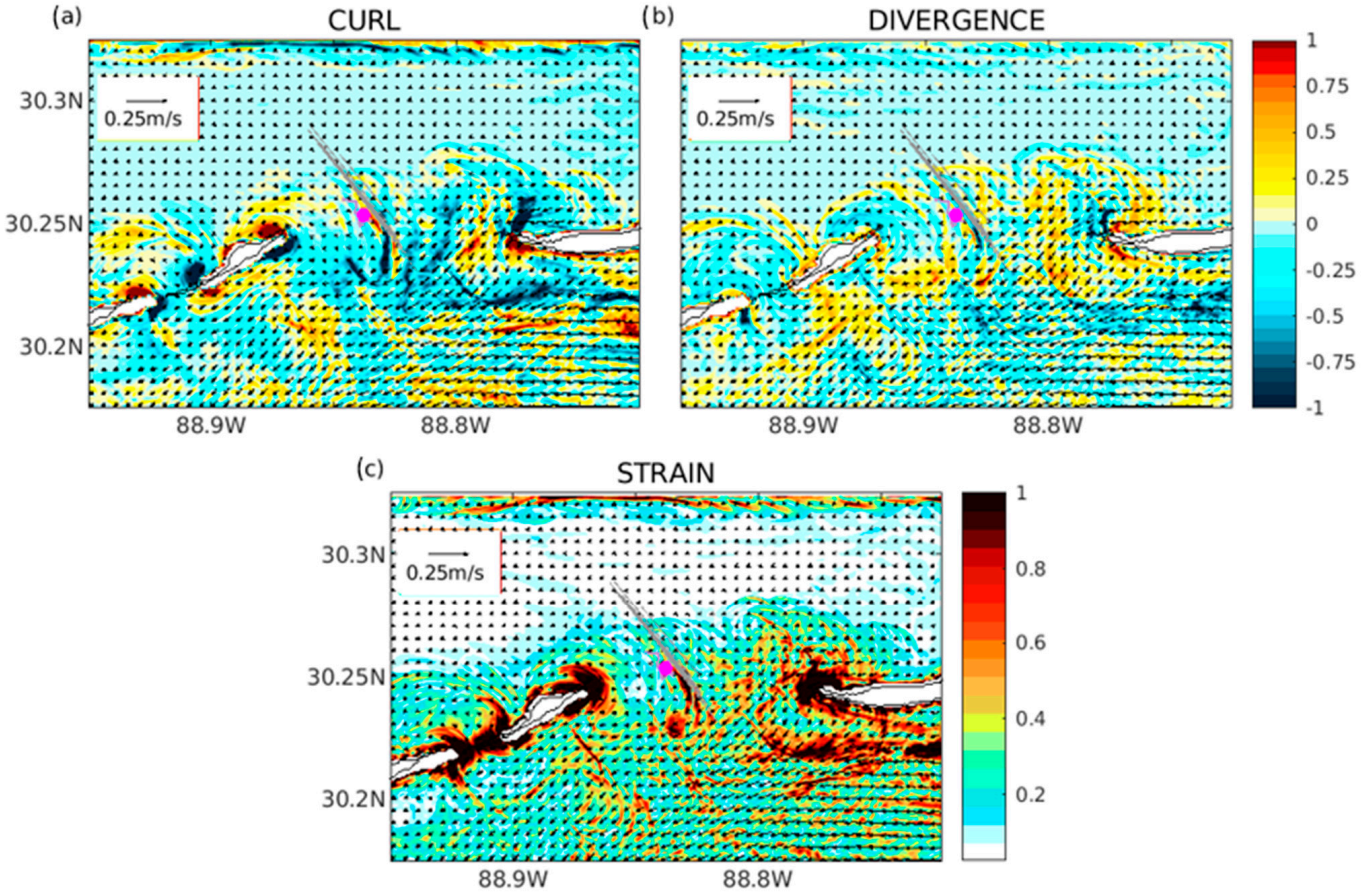

Figure 14. Estimated curl (**a**), divergence (**b**), and strain (**c**) (normalized by the Coriolis parameter f) from the 49 h averaged surface currents of the hydrodynamic model overlaid by the locations of aircraft flights and the R/V Wilson location on 04/05/2018 at 20:00:00 UTC color bars represent magnitudes of curl (**a**), divergence (**b**), and strain (**c**); aircraft flight locations are shown with gray lines, and R/V Wilson location is shown with magenta circle.

This is supported by the model predictions of temperature, salinity, and vertical velocity along the section between islands in Figure 15, which show a clear frontal area with strong vertical upwelling/downwelling circulation cells representing ageostrophic secondary circulation (ASC) cells [29].

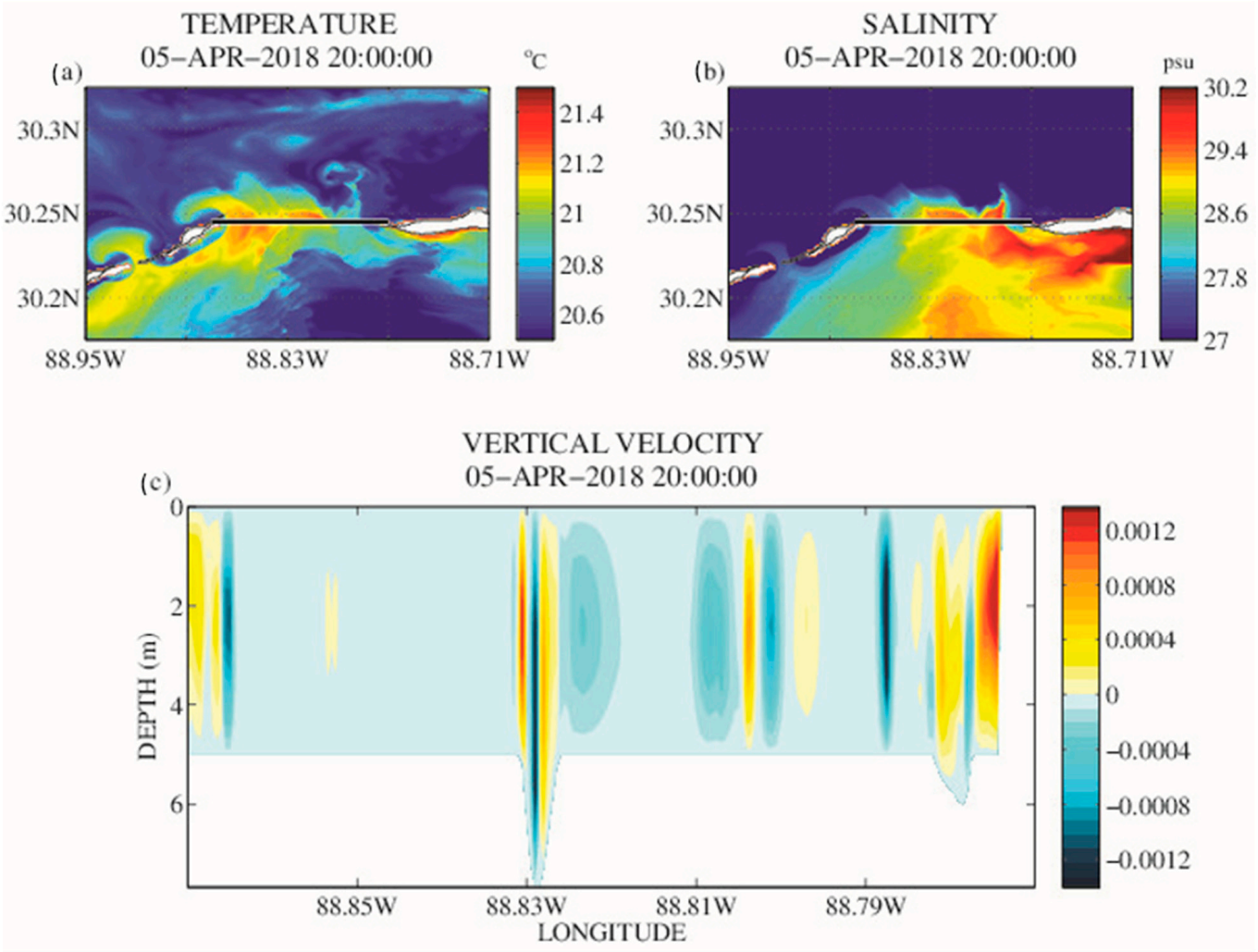

Figure 15. The model predictions of (**a**) temperature, (**b**) salinity, and (**c**) vertical velocity between islands.

5. Conclusions

To study the impact of tides and atmospheric forcing on the characteristics of the coastal convergence zone, in-water instruments were deployed during March and April of 2018 in the Mississippi Sound south of Biloxi, Mississippi, and to the north, south, and within the pass between the Horn and Ship Islands. On 5 April, 1500 UTC, airborne data from the μSHINE sensor detected a front oriented in a roughly west-to-east direction that coincided with the opposing forces of the flood tide and the northerly winds in the morning. As these forces transitioned toward the opposing forces of the ebb tide and southerly winds in the afternoon, about 5 h later (at around 2000 UTC), the front rotated to a north-to-south orientation within the pass. As demonstrated here, the change in the front orientation follows the wind reversal and changes from flood tide to ebb tide. In accordance with the previous analysis[2], there was also surface cooling as more saline surface water was advected into the area. The model surface and subsurface predictions previously demonstrated[2] that there was a combination of advection of upwelled, more saline water into the area, as well as mixing of the water column due to wind, surface cooling, and tidal mixing during 04/04/18–04/05/18. This also formed and sharpened the front observed by aircraft imagery and by ship surveys on 04/05/18.

In the present paper, we demonstrated that the model's high values of curl, divergence, and strain coincide with the flight lines oriented along the front in north–south direction on 5 April 2000, UTC, indicating a good correspondence between the model and observed front locations. In addition, model surface temperature and salinity plots show a strong gradient

at about 88.83 W longitude along the 30.24 N latitude transect, which is also the location of the front identified in the 20:13:37 UTC μSHINE image. The model vertical velocity shows strong upwelling and downwelling at the 88.83 W longitude location across the 30.24 N latitude transect. This presence of ageostrophic secondary circulation cells [14] indicates that submesoscale processes, along with atmospheric forcing and tides, contributed to the front development.

The conclusion of this work is that raw μSHINE data can be atmospherically corrected using ASD radiometer measurements as input to the Empirical Line Calibration. The resulting atmospherically corrected reflectance fields can be converted to VIIRS relative spectral response and then processed by APS to generate bio-optical ocean color products. These products were used to confirm the characteristics of a front at opposing wind and tidal forces and track its transition from a west-to-east front coincident with a flood tide and northerly winds to a north-to-south front positioned between Horn and Ship Island.

The UAV tiles were small, which makes it difficult for each individual tile to provide comprehensive information about the frontal region. However, the process of using the ELC μSHINE as in situ data for the ELC of UAV data is presented here as a methodology that can be used to atmospherically correct UAV data in future projects.

Model runs were able to recreate this transitioning front using tidal and wind information. Therefore, this modeling process can be used to explore fronts at other locations where tidal and wind forces converge. The identification of spikes in the upwelling and downwelling circulations at these locations was found to be consistent with the locations identified in the μSHINE image fields.

Further work can be carried out with this dataset to explore the impact that the bathymetry of the Dog Key Pass and Little Dog Key Pass, which exist between Ship and Horn Islands, has on the ultimate north-to-south orientation of the front after 2000 UTC. This work establishes methodologies for exploring these coastal convergence zones coincident with tidal and wind forces.

Author Contributions: Conceptualization, M.D.L. and R.G; methodology, M.D.L., R.W.G.J., H.W., G.B.S., W.D.M., T.A.S. and I.S.; investigation, M.D.L., R.W.G.J., G.B.S., W.D.M. and H.W.; formal analysis, all; validation, S.C., T.A.S., I.S. and D.W.; software, M.D.L., S.C., T.A.S., I.S., W.D.M. and D.W.; visualization, all; writing—original draft preparation, M.D.L.; writing—review and editing, all; project administration. M.D.L. and R.W.G.J.; funding acquisition, R.W.G.J. All authors have read and agreed to the published version of the manuscript.

Funding: This research was funded by the Naval Research Laboratory project, Integrated Coastal Bio-Optical Dynamics: Impact of Atmospheric and Tidal Fronts (Program Element 61153N).

Data Availability Statement: The volume of satellite, airborne, and UAV data files, in addition to the model runs analyzed in this paper are stored on file systems of the US Naval Research Laboratory and will be made available to members of the scientific community upon request. To obtain the data please contact the corresponding author.

Acknowledgments: We thank Ian Martens, Andrew Quaid, Wesley Goode, and Joel Wesson for invaluable assistance with instrumentation and data collection. We also thank the captains and crews of the R/V Point Sur and the R/V Wilson for their support during the field operations, and Sky Andrew, Matt Wallace, and Marcus Apple (PrecisionHawk, Inc.) for collection of the UAV imagery. This article has been approved for public release by NGA (22-792).

Conflicts of Interest: The authors declare no conflicts of interests. The funders had no role in the design of the study; in the collection, analyses, or interpretation of data; in the writing of the manuscript, or in the decision to publish the results.

References

1. Gould, R.W.; Anderson, S.; Lewis, M.D.; Miller, W.D.; Shulman, I.; Smith, G.B.; Smith, T.A.; Wang, D.W.; Wijesekera, H.W. Assessing the Impact of Tides and Atmospheric Fronts on Submesoscale Physical and Bio-Optical Distributions near a Coastal Convergence Zone. *Remote Sens.* **2020**, *12*, 553. [CrossRef]
2. Martinolich, P.M. *Automated Processing System User's Guide Version 6.12.0*; Naval Research Laboratory: Washington, DC, USA, 2019.
3. Baith, K.; Lindsay, R.; Fu, G.; McClain, C.R. Data analysis system developed for ocean color satellite sensors. *Eos Trans. Am. Geophys. Union* **2001**, *82*, 202. [CrossRef]
4. Zhou, L.; Divakarla, M.; Liu, X.; Layns, A.; Goldberg, M. An Overview of the Science Performances and Calibration/Validation of Joint Polar Satellite System Operational Products. *Remote Sens.* **2019**, *11*, 698. [CrossRef]
5. Justice, C.O.; Vermote, E.; Townshend, J.R.G.; Defries, R.; Roy, D.P.; Hall, D.K.; Salomonson, V.V.; Privette, J.L.; Riggs, G.; Strahler, A.; et al. The Moderate Resolution Imaging Spectroradiometer (MODIS): Land remote sensing for global change research. *IEEE Trans. Geosci. Remote Sens.* **1998**, *36*, 1228–1249. [CrossRef]
6. Kitch, T. NOAA Center for Operational Oceanographic Products and Services. 2018. Available online: https://oceanservice.noaa.gov/annualreport/2018/coops.html (accessed on 22 May 2024).
7. Minor, E.C.; James, E.; Austin, J.A.; Nelson, V.; Lusk, R.; Mopper, K. A preliminary examination of an in situ dual dye approach to measuring light fluxes in lotic systems. *Limnol. Oceanogr. Methods* **2013**, *11*, 631–642. [CrossRef]
8. Legleiter, C.J.; Manley, P.V.; Erwin, S.O.; Bulliner, E.A. An Experimental Evaluation of the Feasibility of Inferring Concentrations of a Visible Tracer Dye from Remotely Sensed Data in Turbid Rivers. *Remote Sens.* **2019**, *12*, 57. [CrossRef]
9. Savelyev, I.; Miller, W.D.; Sletten, M.; Smith, G.B.; Savidge, D.K.; Frick, G.; Menk, S.; Moore, T.; De Paolo, T.; Terrill, E.J.; et al. Airborne Remote Sensing of the Upper Ocean Turbulence during CASPER-East. *Remote Sens.* **2018**, *10*, 1224. [CrossRef]
10. Jarosz, E.; Wijesekera, H.W.; Teague, W.J.; Fribance, D.B.; Moline, M.A. Observations on stratified flow over a bank at low Froude numbers. *J. Geophys. Res. Ocean.* **2014**, *119*, 6403–6421. [CrossRef]
11. Mobley, C.D. Estimation of the remote-sensing reflectance from above-surface measurements. *Appl. Opt.* **1999**, *38*, 7442–7455. [CrossRef]
12. Mueller, J.L.; Morel, A.; Frouin, R.; Davis, C.; Arnone, R.; Carder, K.; Lee, Z.P.; Steward, R.G.; Hooker, S.; Mobley, C.D.; et al. *Ocean Optics Protocols For Satellite Ocean Color Sensor Validation*; NASA/TM-2003-21621/Rev-Vol III; Goddard Space Flight Space Center: Greenbelt, MD, USA, 2003. [CrossRef]
13. Gould, R.W.; Arnone, R.A.; Sydor, M. Absorption, Scattering, and, Remote-Sensing Reflectance Relationships in Coastal Waters: Testing a New Inversion Algorith. *J. Coast. Res.* **2001**, *17*, 328–341.
14. Röttgers, R.; McKee, D.; Woźniak, S.B. Evaluation of scatter corrections for ac-9 absorption measurements in coastal waters. *Methods Oceanogr.* **2013**, *7*, 21–39. [CrossRef]
15. WETLabs. *ac Meter Protocol Document, ac Meter Protocl (acprot)*; Revision Q 20 April 2011; WET Labs, Inc.: St. Philomath, OR, USA, 2011.
16. Zaneveld, J.R.V.; James, C.K.; Casey, C.M. Scattering error correction of reflection-tube absorption meters. In Proceedings of the SPIE, Bergen, Norway, 13–15 June 1994; Volume 2258, pp. 44–55. [CrossRef]
17. Pope, R.M.; Fry, E.S. Absorption spectrum (380–700 nm) of pure water. II. Integrating cavity measurements. *Appl. Opt.* **1997**, *36*, 8710–8723. [CrossRef] [PubMed]
18. Werdell, P.J.; McKinna, L.I.W.; Boss, E.; Ackleson, S.G.; Craig, S.E.; Gregg, W.W.; Lee, Z.; Maritorena, S.; Roesler, C.S.; Rousseaux, C.S.; et al. An overview of approaches and challenges for retrieving marine inherent optical properties from ocean color remote sensing. *Prog. Oceanogr.* **2018**, *160*, 186–212. [CrossRef] [PubMed]
19. Guo, Y.; Senthilnath, J.; Wu, W.; Zhang, X.; Zeng, Z.; Huang, H. Radiometric Calibration for Multispectral Camera of Different Imaging Conditions Mounted on a UAV Platform. *Sustainability* **2019**, *11*, 978. [CrossRef]
20. Yang, G.; Li, C.; Wang, Y.; Yuan, H.; Feng, H.; Xu, B.; Yang, X. The DOM Generation and Precise Radiometric Calibration of a UAV-Mounted Miniature Snapshot Hyperspectral Imager. *Remote. Sens.* **2017**, *9*, 642. [CrossRef]
21. Roberts, D.A.; Yamaguchi, Y.; Lyon, R.J.P. Calibration of Airborne Imaging Spectrometer Data to Percent Reflectance Using Field Spectral Measurements. In Proceedings of the 19th International Symposium on Remote Sensing of Environment, Ann Arbor, MI, USA, 21–25 October 1985.
22. Davis, C.O.; Bowles, J.; Leathers, R.A.; Korwan, D.; Downes, T.V.; Snyder, W.A.; Rhea, W.J.; Chen, W.; Fisher, J.; Bissett, W.P. Ocean PHILLS hyperspectral imager: Design, characterization, and calibration. *Opt. Express* **2002**, *10*, 210–221. [CrossRef]
23. Gordon, H.R.; Wang, M. Retrieval of water-leaving radiance and aerosol optical thickness over the oceans with SeaWiFS: A preliminary algorithm. *Appl. Opt.* **1994**, *33*, 443–452. [CrossRef] [PubMed]
24. Ahmad, Z.; Franz, B.A.; McClain, C.R.; Kwiatkowska, E.J.; Werdell, J.; Shettle, E.P.; Holben, B.N. New aerosol models for the retrieval of aerosol optical thickness and normalized water-leaving radiances from the SeaWiFS and MODIS sensors over coastal regions and open oceans. *Appl. Opt.* **2010**, *49*, 5545–5560. [CrossRef] [PubMed]
25. Franz, B.A.; Bailey, S.W.; Werdell, P.J.; McClain, C.R. Sensor-independent approach to the vicarious calibration of satellite ocean color radiometry. *Appl. Opt.* **2007**, *46*, 5068–5082. [CrossRef]
26. Bailey, S.W.; Hooker, S.B.; Antoine, D.; Franz, B.A.; Werdell, P.J. Sources and assumptions for the vicarious calibration of ocean color satellite observations. *Appl. Opt.* **2008**, *47*, 2035–2045. [CrossRef]

27. Pierce, B. Viewing Geometry Module. University of Wisconsin-Madison. 2022. Available online: https://svn.ssec.wisc.edu/repos/cloud_team_cr/trunk/viewing_geometry_module.f90 (accessed on 22 May 2024).
28. NOAA National Geophysical Data Center. *2001: U.S. Coastal Relief Model Vol.4—Central Gulf of Mexico*; NOAA National Centers for Environmental Information: Asheville, NC, USA, 2001. [CrossRef]
29. Shulman, I.; Penta, B.; Richman, J.; Jacobs, G.; Anderson, S.; Sakalaukus, P. Impact of submesoscale processes on dynamics of phytoplankton filaments. *J. Geophys. Res. Ocean.* **2015**, *120*, 2050–2062. [CrossRef]